Angular Velocity of Kolmogorov-Scale Fibers as Proxy for Turbulent Dissipation

Domenico Zaza,[1,2] Vlad Giurgiu,[1] Michele Iovieno,[3] and Alfredo Soldati[1,2,*]
[1]*Institute of Fluid Mechanics and Heat Transfer, TU Wien, 1060 Vienna, Austria*
[2]*Polytechnic Department of Engineering and Architecture, Università degli Studi di Udine, 33100 Udine, Italy*
[3]*Department of Mechanical and Aerospace Engineering, Politecnico di Torino, 10129 Turin, Italy*

(Received 28 October 2025; accepted 2 January 2026; published 3 February 2026)

We introduce a fiber-based method to directly measure turbulent energy dissipation. Combining original measurements of the full-body rotation—tumbling and spinning—of short, Kolmogorov-scale fibers in turbulent channel flow with direct numerical simulations using a point-fiber model, we show that the mean-square angular velocity closely reproduces the mean dissipation rate. The method is accurate both in the nearly homogeneous turbulence of the channel center and in the logarithmic layer, with a mean deviation below 6%, demonstrating that Kolmogorov-scale fibers provide a robust and reliable tool for quantifying dissipation.

DOI: 10.1103/kcmw-5dph

Introduction—In turbulent flows, the mean rate at which viscosity converts the kinetic energy of turbulent fluctuations into heat is a fundamental quantity for both practical applications [1–3] and theoretical formulations [4–7]. It is defined as $\langle\epsilon\rangle = 2\nu\langle S'_{ij}S'_{ij}\rangle$ [8], where ν is the kinematic viscosity and $S'_{ij} = S_{ij} - \langle S_{ij}\rangle$ is the fluctuating part of the strain–rate tensor, with $S_{ij} = 1/2(A_{ij} + A_{ji})$ and $A_{ij} = \partial u_i/\partial x_j$ the velocity gradient tensor. The brackets $\langle\cdot\rangle$ denote ensemble averaging and the prime $'$ indicates the fluctuations.

Direct measurements of $\langle\epsilon\rangle$ remain challenging [9], since evaluating the velocity gradient tensor requires three-dimensional velocity field acquisitions [10,11] with spatial resolution on the order of the Kolmogorov length scale, $\eta = (\nu^3/\langle\epsilon\rangle)^{1/4}$. At high Reynolds numbers, this requirement poses major difficulties, motivating the development of alternative approaches to estimate $\langle\epsilon\rangle$ from proxy measurements [1].

Recently, the possibility of using rigid fibers to measure $\langle\epsilon\rangle$ has been enabled by advanced optical tracking [12,13], combined with their sensitivity to the velocity gradient tensor [9,14–17]. Measurements of the full rotational kinematics of fibers [12,13], both tumbling and spinning, advance earlier methods limited to tumbling only [14–16,18] enabling the mean-square angular velocity of nearly inertia-free fibers to serve as an accurate proxy for $\langle\epsilon\rangle$.

In the Stokes-flow regime, the mean-square angular velocity $\langle\boldsymbol{\omega}_p^2\rangle$ of fibers follows from Jeffery's equation for inertialess ellipsoids [19]:

$$\langle\boldsymbol{\omega}_p^2\rangle = \frac{1}{4}\langle\boldsymbol{\omega}^2\rangle + \lambda^2\langle(\mathbf{p}\times\mathbf{Sp})^2\rangle + \lambda\langle\boldsymbol{\omega}\cdot(\mathbf{p}\times\mathbf{Sp})\rangle, \tag{1}$$

where $\mathbf{p}$ is the unit vector along the ellipsoid's symmetry axis, $\mathbf{S}$ the strain-rate tensor, $\boldsymbol{\omega}$ the fluid vorticity, and $\lambda = (\alpha^2 - 1)/(\alpha^2 + 1)$, with $\alpha = \ell/d$ the aspect ratio (ℓ and d denote the major and minor axes, respectively).

With simulations of Jeffery's ellipsoids dispersed in homogeneous isotropic turbulence (HIT), Ref. [17] showed that the second and third terms in Eq. (1) nearly cancel, making $\langle\boldsymbol{\omega}_p^2\rangle$ essentially independent of particle shape (λ) and dominated by enstrophy, $\langle\boldsymbol{\omega}_p^2\rangle \approx \frac{1}{4}\langle\boldsymbol{\omega}^2\rangle$. In HIT, the mean vorticity vanishes, implying that $\langle\boldsymbol{\omega}_p^2\rangle \approx \frac{1}{4}\langle\boldsymbol{\omega}'^2\rangle$. Applying the first Betchov constraint [20], this relation simplifies to $\langle\boldsymbol{\omega}_p^2\rangle \approx \frac{1}{4}\langle\epsilon\rangle/\nu$. Kinematically, this implies that the ellipsoids' rotational timescale $\langle\boldsymbol{\omega}_p^2\rangle^{-1/2}$ scales with the timescale of Kolmogorov-sized eddies, $\tau_\eta = (\nu/\langle\epsilon\rangle)^{1/2}$.

For fibers with lengths in the inertial subrange, this scaling remains valid [17] if τ_η is replaced by the eddy turnover time at scale ℓ, $\tau_\ell = \langle\overline{A'}^{\ell}_{ij}\overline{A'}^{\ell}_{ij}\rangle^{-1/2}$, where $\overline{A'}^{\ell}_{ij}$ is the fluctuating velocity gradient tensor filtered at the ellipsoid length [21]. Since $\langle\overline{A'}^{\ell}_{ij}\overline{A'}^{\ell}_{ij}\rangle = \mathcal{C}\tau_\eta^{-2}(\ell/\eta)^{-4/3}$ [8,21], it follows that $\langle\boldsymbol{\omega}_p^2\rangle \approx \frac{1}{4}\mathcal{C}\tau_\eta^{-2}(\ell/\eta)^{-4/3}$, which is equivalent to $\langle\boldsymbol{\omega}_p^2\rangle \approx \frac{1}{4}\mathcal{C}\ell^{-4/3}\langle\epsilon\rangle^{2/3}$. Here the multiplicative constant is $\mathcal{C} = a_f C_K \approx 11.22$, with $C_K \approx 1.58$ Kolmogorov's constant for the three-dimensional energy spectrum [22], and $a_f \approx 7.10$ a filter-dependent factor for a Gaussian kernel [8].

---

[*] Contact author: alfredo.soldati@tuwien.ac.at

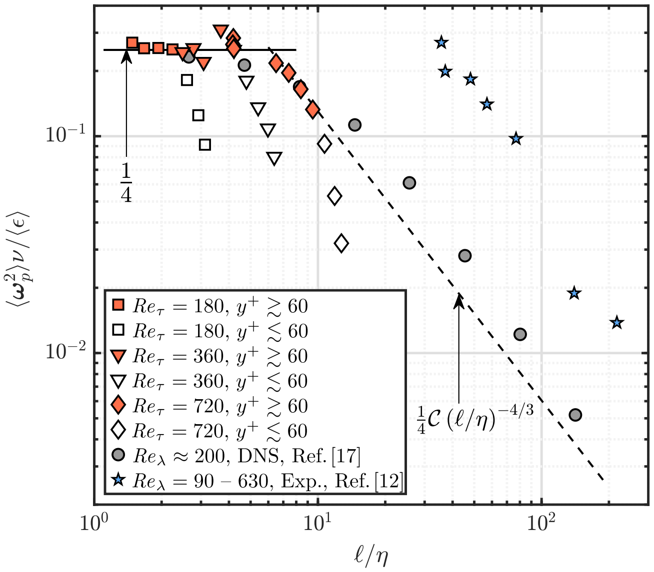

FIG. 1. Measured mean-square angular velocity of fibers, $\langle \boldsymbol{\omega}_p^2 \rangle$, as a function of the ratio between the nominal fiber length, ℓ, and the local Kolmogorov length scale, η. Various Re_τ are showcased ($Re_\tau = 180$, 360, 720), with solid orange markers denoting results for $y^+ \gtrsim 60$ and open markers indicating results for $y^+ \lesssim 60$. The angular velocities are rescaled by the local Kolmogorov time scale $\tau_\eta = (\nu/\langle \epsilon \rangle)^{1/2}$, with $\langle \epsilon \rangle$ obtained from DNS at similar Re_τ ($Re_\tau = 180$, 360, and 700). Overlain, the scalings suggested by Ref. [17] for ℓ in the dissipative range ($\langle \boldsymbol{\omega}_p^2 \rangle \tau_\eta^2 \approx 1/4$, solid line) and for ℓ in the inertial subrange ($\langle \boldsymbol{\omega}_p^2 \rangle \tau_\eta^2 \approx 1/4\mathcal{C}(\ell/\eta)^{-4/3}$, with $\mathcal{C} = 11.22$, dashed line) are also shown. The mean-square angular velocities reported by Ref. [12] for rods with aspect ratio $\alpha = 10.8$ and those computed by Ref. [17] for spherical particles ($\alpha = 0$) are also included.

This leads to the question of whether the kinematic principle and its implication of measuring $\langle \epsilon \rangle$ using $\langle \boldsymbol{\omega}_p^2 \rangle$, observed thus far only in numerical simulations in HIT, can be confirmed experimentally. Furthermore, can this approach be used in wall-bounded flows, beyond the assumptions of statistical homogeneity and isotropy?

In this Letter—To address these questions, both experimental and numerical evidence of the mean-square angular velocity of slender fibers suspended in turbulent channel flow are provided. Considering fibers with negligible inertia and lengths between 1.5η and 13η, this study presents the first estimation of the mean turbulent dissipation rate based on measurements of the full angular velocity of fibers, introducing a novel method referred to as fiber-based dissipation measurement (FDM).

The canonical configuration of a turbulent channel flow (TCF) provides an ideal test case for exploring the applicability of the FDM method: near the channel centerline, turbulence can be regarded as approximately homogeneous and isotropic [23], allowing direct evaluation of the predictions $\langle \boldsymbol{\omega}_p^2 \rangle \approx 1/4\tau_\eta^{-2}$ and $\langle \boldsymbol{\omega}_p^2 \rangle \approx 1/4\tau_\ell^{-2}$ suggested in HIT [17] for the dissipative and inertial subrange, respectively. Toward the wall, the increasing anisotropy and inhomogeneity offer conditions to examine the presented principle beyond its assumptions.

Experimental and numerical setup—The measurements were conducted in the TU Wien Turbulent Water Channel facility [24] at a mean water temperature of 20.2 °C. A new experimental dataset—including two shear Reynolds numbers, $Re_\tau = 180$ and 360, defined as $Re_\tau = u_\tau h/\nu$, with u_τ friction velocity—was obtained, complementing previously published data at $Re_\tau = 720$ [13]. The kinematic viscosity and channel half height were $\nu = 1\ \mathrm{mm^2\,s^{-1}}$ and $h = 40$ mm, respectively.

Fibers used in these experiments were slightly curved and identical to those in Ref. [13], with density $\rho_f = 1.15\ \mathrm{g\,cm^{-3}}$, length $\ell = 1.2$ mm, and diameter $d = 10\ \mu\mathrm{m}$. The resulting aspect ratio was $\alpha = 120$. Under the present flow conditions, the fibers behave as rigid, inertialess, and effectively straight tracer fibers [13]. Note that their slightly curved shape is exploited to measure their full angular velocity, including the spinning rate, following Ref. [13].

Complementary direct numerical simulations (DNS) of turbulent channel flow laden with prolate ellipsoids [25], having an aspect ratio $\alpha = 120$, were conducted at $Re_\tau = 180$, 360, and 700. The translational and rotational motion of the ellipsoids was computed within a Lagrangian point-particle framework [25] by time integrating the equations of rigid-body motion described in Ref. [26].

To account for the finite-length effects of the experimental fibers while retaining the point-particle formulation, the simulations adopted the approach of Ref. [17]: the hydrodynamic torque on each ellipsoid was evaluated from a spatially filtered velocity-gradient field, $\bar{A}_{ij}^{\ell}$, sampled at the particle center. As detailed in Ref. [26], $\bar{A}_{ij}^{\ell}$ was obtained by filtering A_{ij} at the experimental fiber length ($\ell/h = 3 \times 10^{-2}$) using an isotropic Gaussian kernel. A small Stokes number, $St^+ = 0.35$, defined as the ratio of the particle response time [25] to the viscous timescale $\tau_\nu = \nu/u_\tau^2$, ensures that the ellipsoids behave as translational and rotational tracers in all simulations.

Results and discussions—Figure 1 shows the measured mean-square angular velocity of the fibers, rescaled by the local Kolmogorov timescale, as a function of ℓ/η. While the fibers have a fixed length, η decreases with increasing Re_τ, so that, relative to the scales of turbulence, the fibers span the dissipative range ($\ell \lesssim 6\eta$) and the onset of the inertial subrange ($\ell \gtrsim 6\eta$). The results are reported for three Re_τ (squares for $Re_\tau = 180$, triangles for $Re_\tau = 360$, diamonds for $Re_\tau = 720$). Since Ref. [39] finds deviations of velocity gradient quantities in TCF with respect to HIT starting below $y^+ \sim 60$, measurements in the channel core ($y^+ \gtrsim 60$, solid orange markers) are distinguished from those in the near-wall region ($y^+ \lesssim 60$, open markers).

In the region $y^+ \gtrsim 60$, the fibers' mean-square angular velocity $\langle \boldsymbol{\omega}_p^2 \rangle$ closely follows the scaling laws suggested for HIT [17] in both the dissipative range and the inertial subrange. Specifically, in the dissipative range the scaling is constant with ℓ/η, and in the inertial subrange it follows the $-4/3$ law. Both scalings include the factor $1/4$, as predicted by Jeffery's equation (1) and consistent with the fact that the local angular velocity of a fluid element is half the magnitude of the vorticity vector.

This close agreement has two main implications. For most of the channel height, (i) the mean-square angular velocity of slender fibers with lengths in either the dissipative or inertial range provides an accurate estimate of the local mean turbulent dissipation rate, as $\langle\epsilon\rangle \approx 4\nu\langle\boldsymbol{\omega}_p^2\rangle$ and $\langle\epsilon\rangle \approx 8\mathcal{C}^{-3/2}\langle\boldsymbol{\omega}_p^2\rangle^{3/2}\ell^2$, respectively. The FDM method achieves remarkable accuracy, with a mean relative error of 5.4% across all Reynolds numbers considered (specifically, 6% in the dissipative range and 3% in the inertial subrange). Near the wall ($y^+ \lesssim 60$), however, $\langle\boldsymbol{\omega}_p^2\rangle$ progressively departs from both scaling laws (open markers in Fig. 1), with deviations exceeding 25% for all Re_τ, reflecting the emergence of small-scale anisotropy [39]. (ii) The rotational kinematics of fibers, governed solely by the rotation of eddies of comparable size, are essentially independent of λ and nearly indistinguishable from those of spheres, consistent with numerical results in Ref. [17] (gray circles in Fig. 1). Owing to this near shape invariance—absent when considering tumbling and spinning rates separately [25]—$\langle\boldsymbol{\omega}_p^2\rangle$ emerges as a more robust estimator of $\langle\epsilon\rangle$ than the individual rotational components.

The near shape invariance of $\langle\boldsymbol{\omega}_p^2\rangle$ has been attributed, for Jeffery's ellipsoids in HIT, to its statistical independence from the fiber orientation relative to the eigenframe of A_{ij} [17]. In contrast, spinning or tumbling alone retain an orientation dependence that varies with both the scale sampled by the fibers and their aspect ratio [17]. Prior estimates of $\langle\epsilon\rangle$ based solely on the mean-square tumbling rate [9,15], which commonly assume random fiber orientation relative to A_{ij}, can introduce errors up to 20% in direct measurements of $\langle\epsilon\rangle$ [9,40].

For reference, comparison with previous measurements for longer, thicker ($\alpha = 10.8$) fibers (blue stars in Fig. 1) shows an offset relative to the present data, consistent with finite-diameter effects reported in Ref. [12].

As discussed earlier, the kinematic principle whereby, in HIT, fibers' angular velocity scales with the turnover time of eddies of comparable size—confirmed in Fig. 1 for $y^+ \gtrsim 60$—rests on the validity of Jeffery's model in describing the rotational kinematics of fibers, and on the near balance between the strain-induced and mixed vorticity-strain contributions it contains. The remainder of this Letter is therefore dedicated to the examination of these two underlying aspects.

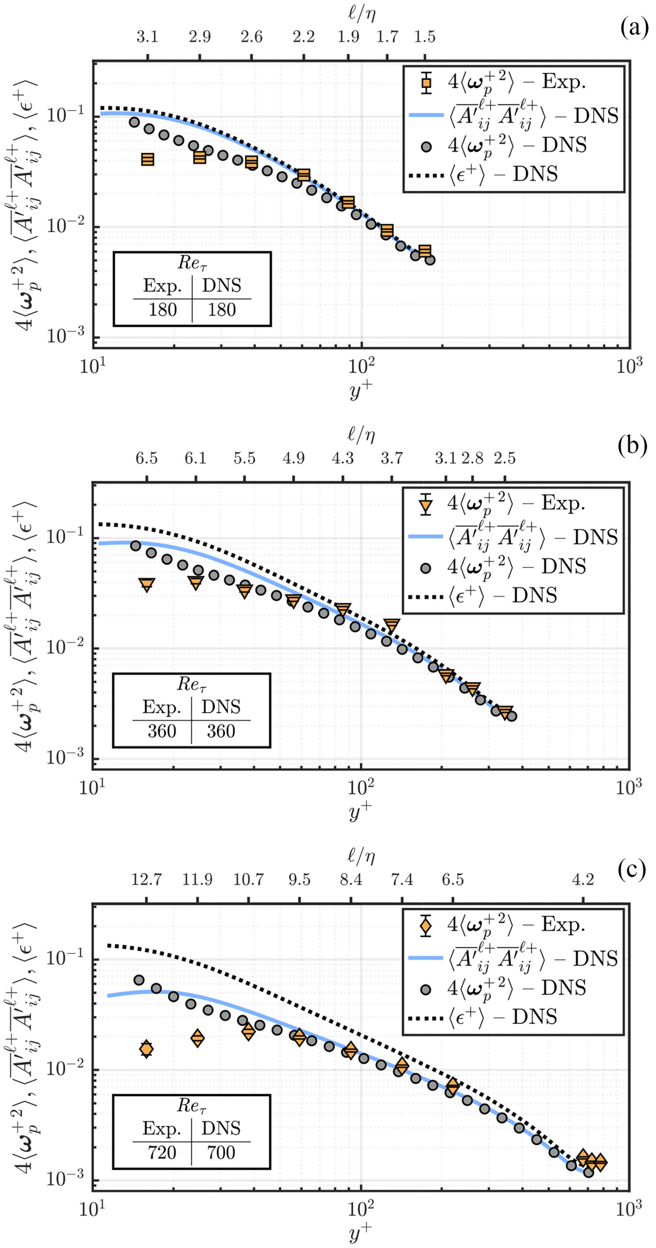

FIG. 2. Mean-square angular velocity of both numerical (gray circles) and experimental (yellow markers) fibers plotted together with the numerical dissipation rate $\langle\epsilon^+\rangle$ (dashed line) and magnitude of the fluctuating gradient tensor $\langle\bar{A}'^{\ell+}_{ij}\bar{A}'^{\ell+}_{ij}\rangle$ filtered at the experimental fiber length ℓ (solid blue line). Both $\langle\epsilon^+\rangle$ and $\langle\bar{A}'^{\ell+}_{ij}\bar{A}'^{\ell+}_{ij}\rangle$ are obtained from DNS. Results are shown as a function of the wall-normal coordinate, y^+, and have been made dimensionless using inner scales: $\delta_\nu = \nu/u_\tau$ and $\tau_\nu = \nu/u_\tau^2$. Each panel presents different friction Reynolds numbers: (a) $Re_\tau = 180$, (b) $Re_\tau = 360$, and (c) $Re_\tau = 700$ (DNS) and $Re_\tau = 720$ (experiments). The upper horizontal axis reports ℓ/η of the experimental fibers. Error-bars represent confidence intervals at 99% confidence level and have been computed using the bootstrap-based method of Ref. [41].

Figure 2 compares the mean-square angular velocity obtained from experiments (yellow markers) with numerical results for Jeffery's ellipsoids (gray circles) sampling the velocity-gradient tensor filtered at the fiber length ℓ, $\bar{A}^{\ell}_{ij}$, at corresponding Re_τ. The results are shown as functions of y^+ and are nondimensionalized using the viscous length and time scales, δ_ν and τ_ν, as conventionally denoted by the superscript "+." Additionally, $4\langle\boldsymbol{\omega}_p^{+2}\rangle$ is shown to facilitate comparison with the expected scalings. Quantitatively, Figure 2 suggests that the ℓ-filtered Jeffery model for numerical ellipsoids (gray circles) captures the $\langle\boldsymbol{\omega}_p^{+2}\rangle$ of finite-length fibers (yellow markers) from the center line down to $y^+ \approx 20$ at $Re_\tau = 180$ [Fig. 2(a)] and $Re_\tau = 360$ [Fig. 2(b)], and to $y^+ \approx 40$ at the highest Re_τ [Exp. 720, DNS 700; Fig. 2(c)]. Visible deviations consistently appear below $y^+ \approx 2\ell^+$ for all Re_τ investigated (with $\ell^+ = 5.4$, 10.8, and 21.8 at $Re_\tau = 180$, 360, and 720, respectively), indicating that the reduced angular velocities exhibited by the experimental fibers while approaching the wall result from fiber-wall interactions that limit rotation. This near-wall effect is absent in the simulations, where the idealized Jeffery ellipsoids do not experience such geometric constraints.

Confirming earlier observations, for $y^+ \gtrsim 60$ both the ellipsoids and the experimental fibers exhibit a mean-square angular velocity that closely follows the numerical prediction $(\tau_\ell^+)^{-2} = \langle\overline{A'}^{\ell+}_{ij}\overline{A'}^{\ell+}_{ij}\rangle$ (solid blue line). This quantity approaches and saturates to $(\tau_\eta^+)^{-2} = \langle\epsilon^+\rangle$ (dashed line) for lengths $\ell \lesssim 6\eta$, as shown by the upper axis in ℓ/η.

The excellent agreement between numerical and experimental values of $\langle\boldsymbol{\omega}_p^{+2}\rangle$ validates a modeling approach that replaces the local velocity gradient in Jeffery's equation with its spatially filtered counterpart. This formulation effectively captures finite-length effects, bridging the gap between conventional point-particle descriptions and particle-resolved simulations.

Guided by this agreement, we use the numerical simulations to examine the contributions responsible for the scalings and near-wall reduced rotation rates observed in experiments. Recalling Eq. (1), we replace the local strain-rate tensor and vorticity vector, $\mathbf{S}$ and $\boldsymbol{\omega}$, with their counterparts spatially filtered at the fiber length scale ℓ, and decompose the filtered enstrophy term into mean and fluctuating contributions, obtaining

$$\langle\boldsymbol{\omega}_p^2\rangle = \frac{1}{4}\left(\overline{\frac{\mathrm{d}\langle u\rangle}{\mathrm{d}y}}^{\ell}\right)^2 + \frac{1}{4}\langle\overline{\boldsymbol{\omega}'}^{\ell 2}\rangle + \lambda^2\langle(\mathbf{p}\times\bar{\mathbf{S}}^{\ell}\mathbf{p})^2\rangle + \lambda\langle\bar{\boldsymbol{\omega}}^{\ell}\cdot(\mathbf{p}\times\bar{\mathbf{S}}^{\ell}\mathbf{p})\rangle. \quad (2)$$

The relative magnitudes of the contributions on the right-hand side of Eq. (2), evaluated from DNS, are presented in Fig. 3. The contributions are rescaled by $1/(4\tau_\ell^2)$ and plotted as a function of y^+. In order these terms represent the pure effect of mean shear (black stars) and the contribution from fluctuating vorticity (red circles)—neither of which depends on particle orientation or shape—followed by the strain-induced (blue squares) and the mixed strain-vorticity (orange diamonds) contributions. For clarity, the latter is plotted with its sign reversed, so that the degree of cancellation between the two shape-dependent contributions can be directly observed. These two terms depend explicitly on particle shape through λ and account for the relative orientation between fibers, the strain eigenframe, and the vorticity vector. For spherical particles ($\lambda = 0$) the strain-induced and mixed terms vanish, so the mean-square angular velocity reduces to the flow enstrophy alone.

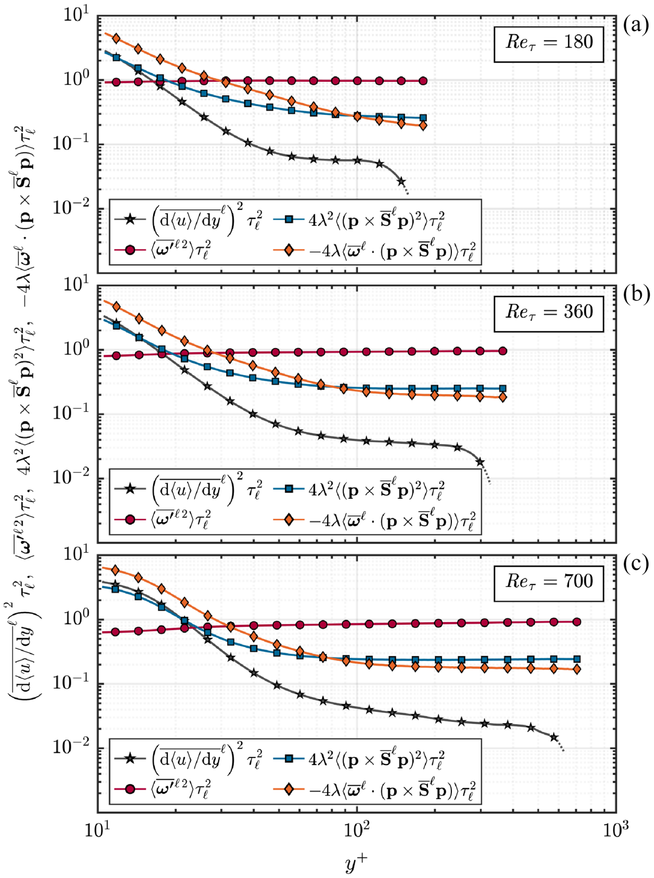

FIG. 3. Relative contributions to the mean-square angular velocity of ellipsoids [Eq. (2)] obtained from DNS: the mean shear $1/4(\overline{\mathrm{d}\langle u\rangle/\mathrm{d}y}^{\ell})^2$ (black stars), the fluctuating enstrophy $1/4\langle\overline{\boldsymbol{\omega}'}^{\ell 2}\rangle$ (red circles), the strain-induced term $\lambda^2\langle(\mathbf{p}\times\bar{\mathbf{S}}^{\ell}\mathbf{p})^2\rangle$ (blue squares), and the cross term $\lambda\langle\bar{\boldsymbol{\omega}}^{\ell}\cdot(\mathbf{p}\times\bar{\mathbf{S}}^{\ell}\mathbf{p})\rangle$ (orange diamonds, plotted with reversed sign). The quantities are rescaled by $1/4\tau_\ell^{-2}$ and plotted against y^+, with each panel corresponding to a different friction Reynolds number: (a) $Re_\tau = 180$, (b) $Re_\tau = 360$, and (c) $Re_\tau = 700$.

Across all Re_τ examined, Fig. 3 shows that $\langle\overline{\boldsymbol{\omega}'}^{\ell 2}\rangle \approx \tau_\ell^{-2}$, indicating that any deviations of the fibers' angular velocity from $\frac{1}{4}\langle\overline{A'}^{\ell}_{ij}\overline{A'}^{\ell}_{ij}\rangle$ must arise from the remaining terms.

At the channel center, where the mean shear is negligible, the strain-induced and mixed contributions nearly cancel, consistent with the findings of Ref. [17] for HIT. Moving toward the wall, the relative contribution of mean shear increases, while the strain-induced and mixed terms continue to partially cancel down to $y^+ \approx 70$ for all Re_τ considered. This balance explains the near shape-invariance of $\langle \boldsymbol{\omega}_p^2 \rangle$ observed in Fig. 1 within the channel core and, together with the weak mean shear, the close agreement with HIT scalings.

As the wall is approached, the balance is progressively disrupted: the negative cross term outweighs the positive strain-induced term, and despite the growing contribution of mean shear, the total normalized contribution falls below unity. This imbalance causes the systematic near-wall deviation of $\langle \boldsymbol{\omega}_p^2 \rangle$ from $1/4\tau_\ell^{-2}$—and, by extension, from $1/4\tau_\eta^{-2}$ when $\ell \lesssim 6\eta$—so that fibers cannot be expected to recover $\langle \epsilon \rangle$ accurately in this region. Approaching the wall, the imbalance between the third and fourth terms in Eq. (2) signals the breakdown of the canonical HIT alignment among the fluid vorticity, the strain eigenframe, and the direction of strongest Lagrangian stretching [42].

Conclusions—A fiber-based dissipation measurement (FDM) provides a direct, experimentally accessible proxy for the mean turbulent energy dissipation rate. Fibers with lengths on the order of the Kolmogorov scale capture the local velocity gradients responsible for dissipation, allowing $\langle \epsilon \rangle$ to be inferred from their angular velocity statistics. Experiments and direct numerical simulations show that, when scaled with the turnover time of eddies of comparable size, the mean-square angular velocity of such fibers yields a nearly shape-independent estimate of $\langle \epsilon \rangle$ for $y^+ \gtrsim 60$, with average relative errors below 6%. The agreement between experiments and simulations across a range of shear Reynolds numbers confirms that Jeffery's model, evaluated using the velocity gradient filtered at the fiber length, accurately accounts for finite-size effects, providing a framework that bridges point-particle and particle-resolved descriptions. The near cancellation between the strain-induced and mixed strain-vorticity contributions to $\langle \boldsymbol{\omega}_p^2 \rangle$ explains the observed shape invariance, while the deviations near the wall arise from the breakdown of HIT-like vorticity-strain alignments. These results establish FDM as a robust approach for quantifying turbulent dissipation in wall-bounded (for $y^+ \gtrsim 60$) and homogeneous flows alike.

Acknowledgments—The authors acknowledge F. Neuwirth and J. Werner for the support in design and construction of the experimental facility, and Giuseppe C. A. Caridi and Eliza Coliban for their contributions in the experimental measurements. V. G. acknowledges the financial support provided by FSE S3 HEaD (Grant No. 1619942002). This research was funded in part by the Austrian Science Fund (FWF) [Grant DOI: 10.55776/P35505] (Grant No. P-35505). A. S. gratefully acknowledges financial support from the European Union-NextGenerationEU PNRR M4.C2.1.1 - PRIN 2022, “The fluid dynamics of interfaces: mesoscale models for bubbles, droplets, and membranes and their coupling to large scale flows” 2022R9B2MW - G53C24000810001. The authors acknowledge ISCRA for awarding this project access to the LEONARDO supercomputer, owned by the EuroHPC Joint Undertaking, hosted by CINECA (Italy). The authors acknowledge the support of LaVision GmbH related to the cameras and software used in the experimental measurements.

Data availability—The data that support the findings of this article are openly available at Ref. [43].

[1] M. Schröder, T. Bätge, E. Bodenschatz, M. Wilczek, and G. Bagheri, Estimating the turbulent kinetic energy dissipation rate from one-dimensional velocity measurements in time, Atmos. Meas. Tech. **17**, 627 (2024).

[2] B. R. Pearson, P.-A. Krogstad, and W. van de Water, Measurements of the turbulent energy dissipation rate, Phys. Fluids **14**, 1288 (2002).

[3] G. Wang, F. Yang, K. Wu, Y. Ma, C. Peng, T. Liu, and L.-P. Wang, Estimation of the dissipation rate of turbulent kinetic energy: A review, Chem. Eng. Sci. **229**, 116133 (2021).

[4] J. C. Vassilicos, Dissipation in turbulent flows, Annu. Rev. Fluid Mech. **47**, 95 (2015).

[5] A. N. Kolmogorov, On the degeneration of isotropic turbulence in an incompressible viscous fluid, Dokl. Akad. Nauk SSSR **31**, 538 (1941).

[6] A. N. Kolmogorov, The local structure of turbulence in incompressible viscous fluids for very large Reynolds numbers, Dokl. Akad. Nauk SSSR **30**, 299 (1941); reprinted in Proc. R. Soc. A **434**, 9 (1991).

[7] A. N. Kolmogorov, Dissipation of energy in isotropic turbulence, Dokl. Akad. Nauk SSSR **32**, 19 (1941).

[8] S. B. Pope, *Turbulent Flows* (Cambridge University Press, Cambridge, England, 2000).

[9] S. Brizzolara, M. E. Rosti, S. Olivieri, L. Brandt, M. Holzner, and A. Mazzino, Fiber tracking velocimetry for two-point statistics of turbulence, Phys. Rev. X **11**, 031060 (2021).

[10] B. W. Zeff, D. D. Lanterman, R. McAllister, R. Roy, E. J. Kostelich, and D. P. Lathrop, Measuring intense rotation and dissipation in turbulent flows, Nature (London) **421**, 146 (2003).

[11] J. A. Mullin and W. J. A. Dahm, Dual-plane stereo particle image velocimetry measurements of velocity gradient tensor fields in turbulent shear flow. I. Accuracy assessments, Phys. Fluids **18**, 035101 (2006).

[12] T. B. Oehmke, A. D. Bordoloi, E. Variano, and G. Verhille, Spinning and tumbling of long fibers in isotropic turbulence, Phys. Rev. Fluids **6**, 044610 (2021).

[13] V. Giurgiu, G. C. A. Caridi, M. De Paoli, and A. Soldati, Full rotational dynamics of plastic microfibers in turbulence, Phys. Rev. Lett. **133**, 054101 (2024).

[14] S. Parsa, E. Calzavarini, F. Toschi, and G. A. Voth, Rotation rate of rods in turbulent fluid flow, Phys. Rev. Lett. **109**, 134501 (2012).

[15] S. Parsa and G. A. Voth, Inertial range scaling in rotations of long rods in turbulence, Phys. Rev. Lett. **112**, 024501 (2014).

[16] S. Bounoua, G. Bouchet, and G. Verhille, Tumbling of inertial fibers in turbulence, Phys. Rev. Lett. **121**, 124502 (2018).

[17] N. Pujara, J.-A. Arguedas-Leiva, C. C. Lalescu, B. Bramas, and M. Wilczek, Shape- and scale-dependent coupling between spheroids and velocity gradients in turbulence, J. Fluid Mech. **922**, R6 (2021).

[18] L. J. Baker and F. Coletti, Experimental investigation of inertial fibres and disks in a turbulent boundary layer, J. Fluid Mech. **943**, A27 (2022).

[19] G. B. Jeffery, The motion of ellipsoidal particles immersed in a viscous fluid, Proc. R. Soc. A **102**, 161 (1922).

[20] R. Betchov, An inequality concerning the production of vorticity in isotropic turbulence, J. Fluid Mech. **1**, 497 (1956).

[21] P. L. Johnson and M. Wilczek, Multiscale velocity gradients in turbulence, Annu. Rev. Fluid Mech. **56**, 463 (2024).

[22] D. A. Donzis and K. R. Sreenivasan, The bottleneck effect and the Kolmogorov constant in isotropic turbulence, J. Fluid Mech. **657**, 171 (2010).

[23] J. Jiménez, Near-wall turbulence, Phys. Fluids **25**, 101302 (2013).

[24] V. Giurgiu, G. C. A. Caridi, M. Alipour, M. De Paoli, and A. Soldati, The TU Wien Turbulent Water Channel: Flow control loop and three-dimensional reconstruction of anisotropic particle dynamics, Rev. Sci. Instrum. **94**, 095101 (2023).

[25] G. A. Voth and A. Soldati, Anisotropic particles in turbulence, Annu. Rev. Fluid Mech. **49**, 249 (2017).

[26] See Supplemental Material at http://link.aps.org/supplemental/10.1103/kcmw-5dph for additional details about (i) experimental data processing, which includes Refs. [13,27,28]; (ii) point-fiber direct numerical simulations, which includes Refs. [17,19,21,25,29–37]; and (iii) the filtered velocity gradient, which includes Refs. [17,30,38].

[27] M. Alipour, Orientation and rotation rates of non-axisymmetric fibers in turbulent channel flow, Ph.D. thesis, Wien, 2021.

[28] G. C. A. Caridi, V. Giurgiu, M. De Paoli, and A. Soldati, Complete solid-body rotation rate measurements of micro-plastic curved fibers in turbulence, Exp. Fluids **66**, 102 (2025).

[29] J. Kim, P. Moin, and R. Moser, Turbulence statistics in fully developed channel flow at low Reynolds number, J. Fluid Mech. **177**, 133 (1987).

[30] C. Canuto, M. Y. Hussaini, A. Quarteroni, and T. A. Zang, *Spectral Methods in Fluid Dynamics* (Springer, Berlin, Heidelberg, 1988).

[31] H. Zhang, G. Ahmadi, F.-G. Fan, and J. B. McLaughlin, Ellipsoidal particles transport and deposition in turbulent channel flows, Int. J. Multiphase Flow **27**, 971 (2001).

[32] P. H. Mortensen, H. I. Andersson, J. J. J. Gillissen, and B. J. Boersma, Dynamics of prolate ellipsoidal particles in a turbulent channel flow, Phys. Fluids **20**, 093302 (2008).

[33] C. Marchioli, M. Fantoni, and A. Soldati, Orientation, distribution, and deposition of elongated, inertial fibers in turbulent channel flow, Phys. Fluids **22**, 033301 (2010).

[34] C. Marchioli and A. Soldati, Rotation statistics of fibers in wall shear turbulence, Acta Mech. **224**, 2311 (2013).

[35] C. Marchioli, L. Zhao, and H. I. Andersson, On the relative rotational motion between rigid fibers and fluid in turbulent channel flow, Phys. Fluids **28**, 013301 (2016).

[36] H. Brenner, The Stokes resistance of an arbitrary particle—IV Arbitrary fields of flow, Chem. Eng. Sci. **19**, 703 (1964).

[37] M. Shapiro and M. Goldenberg, Deposition of glass fiber particles from turbulent air flow in a pipe, J. Aerosol Sci. **24**, 65 (1993).

[38] C. C. Lalescu and M. Wilczek, Acceleration statistics of tracer particles in filtered turbulent fields, J. Fluid Mech. **847**, R2 (2018).

[39] A. Pumir, H. Xu, and E. D. Siggia, Small-scale anisotropy in turbulent boundary layers, J. Fluid Mech. **804**, 5 (2016).

[40] R. Ni, N. T. Ouellette, and G. A. Voth, Alignment of vorticity and rods with Lagrangian fluid stretching in turbulence, J. Fluid Mech. **743**, R3 (2014).

[41] T. J. DiCiccio and B. Efron, Bootstrap confidence intervals, Stat. Sci. **11**, 189 (1996).

[42] L. Zhao and H. I. Andersson, Why spheroids orient preferentially in near-wall turbulence, J. Fluid Mech. **807**, 221 (2016).

[43] D. Zaza, V. Giurgiu, M. Iovieno, and A. Soldati, Data for: Angular velocity of Kolmogorov-scale fibers as proxy for turbulent dissipation, 10.5281/zenodo.17873151 (2026), data set.